

June 2020

Monitoring CO₂ underground storage with the
Riccati equation

Paper no. 4

Cand. Real. Knut Sørsdal

Norway, 2020

Abstract

A study is made of an inversion technique of the Riccati type applied to a CO₂-plume on the Sleipner field in the North sea. This paper employs Q-models and introduce forward and inverse filtering of the data. The solution of the Riccati equation with the the Kolsky-Wang Q-model has been presented in previous papers and is applied here. The linear solution of the wave equation introducing attenuation and dispersion has been studied by Wang. He used a modification of Kolsky's Q-model and applied it on a downward continuation algorithm. I have taken the theory further with a general Q-model and a more elegant inversion. The theory is applied on real seismic data from the Sleipner field. Application on a CO₂-plume will introduce problems concerning velocities and densities that will direct affect the impedance and this is discussed together with the problems of attenuation.

This is an article both on CO₂ and on a special field in seismic called Q-filtering. To start with the first subject we know that higher amounts of CO₂ in the atmosphere has contributed to finding techniques to mitigate the emissions of CO₂. One of those techniques is Carbon Capture and Storage (CCS). CO₂ can be stored in subsurface reservoirs over time. Monitoring and modeling of reservoirs is important to avoid leakage and to predict how the CO₂ could migrate. Modeling is also useful when the seismic interpreter needs a close look at the subsurface data and then Q-filtering is a relevant technique. Seismic from modeling with known parameters can be useful in this connection. I have used the Riccati-equation both for modeling and for inversion to recover the original data used in the seismic theory.

CCS and CO₂ in supercritical state

All over the world there are natural accumulations of CO₂. Natural sources of CO₂ include mantle degassing, metamorphism or dissolution of carbonates, oxidation or bacterial degradation of organic matter, and thermal maturation of hydrocarbons” (Shipton et al., 2004). These natural analogs of CO₂ accumulation are important when deciding a new possible storage site. One can look at the properties and geological structures from the natural reservoirs, and compare these with the observed fluid migration. This will help decrease the possible risk.

The most beneficial way to store CO₂ is in supercritical state, and as we can see on Figure 1 the volume of CO₂ decreases enormously when going from gas phase to supercritical phase. If we have a thermal gradient of 30 degrees per kilometer downwards and we have a pressure gradient of 10,5 MPa per kilometer. Calculating with a CO₂ density of 1,2 kg/m³ (standard pressure and temperature) implies that below a depth of 800 m the CO₂ behaves as a supercritical fluid (Bruant et al., 2002, Halland et al., 2011).

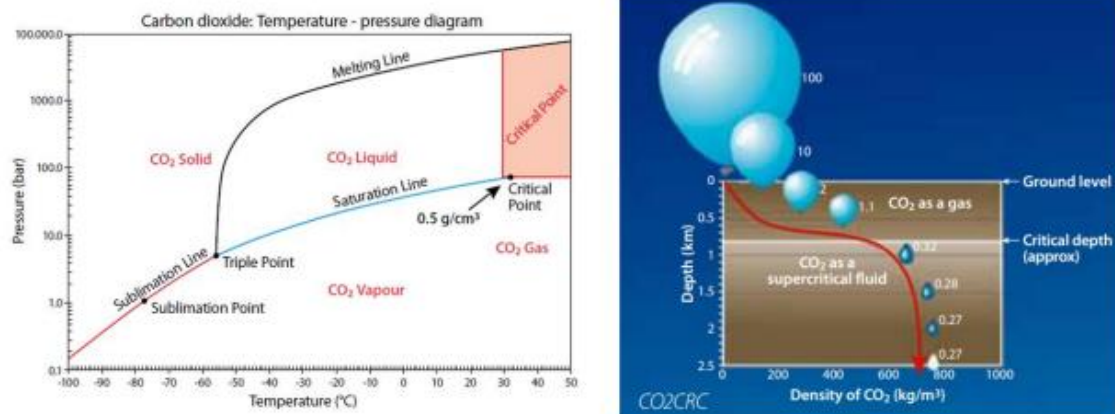


Fig.1. Left: CO₂ temperature – pressure diagram. Right: CO₂ depth – density diagram. (Halland et al (2011)).

So, this article shows modeling of the seismic response from different synthetic models associated with CO₂ underground storage where the parameters are based on real data. And we can concentrate on CO₂ in supercritical phase.

CO₂ saturation, geometry of the models and some other things are all important parameters affecting the seismic result. I have done calculations with a background model that is saturated with CO₂ and received different results depending on saturation percent. Parts of the text about the Sleipner field is taken from a thesis by Nordahl (2015).

Carbon capture, storage and monitoring

Carbon capture and storage (CCS) subsurface is one technique among many to help reduce the amount of CO₂ emissions to the atmosphere. I will take an example. Use of fossil fuels for power generations will increase the amount of CO₂ emissions, but capture of CO₂ in the produced natural gas will help mitigate the emissions.

When the CO₂ is captured and stored in subsurface reservoirs it is important to monitor the behavior of the CO₂ plume. Monitoring of subsurface seismic amplitudes is important to avoid leakage of CO₂ into the sea and atmosphere and to monitor how the plume will develop over time. The primary objective for many papers on this subject is often to get a better understanding of seismic amplitude anomalies associated with subsurface storage of CO₂ over time. However, I will concentrate on real time observation in view of different saturations of CO₂. The models are hypothetical, but the whole background model is based on data from the CO₂ injection site in order to get a realistic setting of the modeling.

Seismic modeling is important in the seismic data acquisition process to give the best possible results considering what the main target is. If the seismic interpreter has problems interpreting the real data, synthetic seismic with known properties can be used for comparison. With modeling, it is also possible to test different survey parameters, like frequencies and different offsets and CO₂-saturation. All these parameters will play a vital role in the resulting seismic. However, I will mainly study the effect of absorption that is introduced as forward Q-filtering. (FQF).

Inversion is an attempt to use modeled data to recover the original data that is consistent with real data. The effect of recovering for absorption is called inverse Q-filtering. (IQF). This paper will both introduce seismic modeling and inversion.

CO₂ and the caprock

CO₂ in a supercritical phase has the behavior of a gas phase and the volume of a liquid phase (Halland et al., 2011). The density of the CO₂ will be smaller than the density of the surrounding reservoir water at shallow depth, less than 5 km (Pruess, 2008). Due to this the molecules of CO₂ will float up in the reservoir (buoyancy effect). The direction of the migration depends on the pressure and permeability. A change in capillary pressure will affect the CO₂ at a much earlier stadium than other fluids. Therefore only a small increase in pressure can make the CO₂ breakthrough the caprock (the capillary pressure is exceeded).

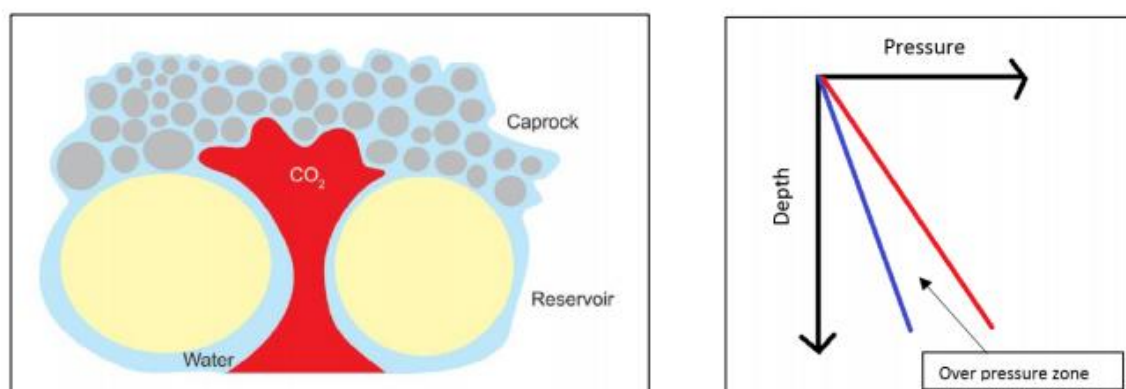


Fig.2. Left: CO₂-migration if the capillary pressure is exceeded. (Hermanrud et al (2009). Right: Hydrostatic gradient (blue) and lithostatic (red).

If a leakage occurs from the reservoir, and the CO₂ starts seeping up to the seafloor, the CO₂ molecules will react with H₂O (water) molecules and form carbonic acid. The acid dissolves and the ions of hydrogen decreases the PH-value, and the ocean water gets more acidic (Bünz et al., 2014). This can have a huge impact on plants and animal life at the seafloor. Leakage from a reservoir offshore is therefore not preferable. The same situation will occur in the reservoir, known as solubility trapping. Microbial organisms convert the CO₂ into CH₄ (methane). This will give an increase in pressure since the compressibility factor for CO₂ is half the size of the compressibility factor for CH₄ (Pruess, 2008). The consequence of increasing pressure is higher risk of leakage.

If the CO₂ has escaped from the reservoir and is migrating, it can be self-enhancing. If the reservoir water gets in contact with the migrating CO₂, the water will become acidic. This will decrease the PH value and cause dissolution of minerals, and the migration pathways for the CO₂ become greater since the permeability increases (Pruess, 2008). The hydrostatic pressure is important to mention, and is defined as the pressure created by the water column above while the lithostatic is pressure created by the weight of the water column and the sediments above. Rapid sedimentation may cause overpressure since the water occupying the pores of the rock does not have time to escape. If the pressure is higher than the capillary entry pressure of the caprock, fluids will break through the caprock and start migrating towards a lower pressure zone.

When sedimentation is in a normal rate, the pore pressure is always in equilibrium with the hydrostatic pressure, and the water has time to escape.

Deep saline aquifers are probably the best way of storing CO₂ (Halland et al., 2011). The definition of a saline aquifer are a reservoir rock with high porosity and permeability (Bentham and Kirby, 2005).

The connection between the grains is important, if the pores are closed or open. Open pores will give higher permeability, and decrease the risk of fracturing of the reservoir rock due to overpressure. The high porosity indicates more empty space between the grains and hence more space for storing CO₂. The permeability allows the stored fluid to migrate within the reservoir rock. When storing in a rock with low permeability the pressure does not have time to stabilize, and this can lead to an overpressure zone close to the injection well (Holloway, 2005).

The formation known as the caprock of the CO₂ reservoir is from Pliocene age in the Nordland group, also called the Nordland shale. The unit known as the Nordland shale (Pliocene shale) was deposited in a deep marine environment resulting in a lowpermeable mudstones with sand in between (Karstens and Berndt, 2015). The unit assumed to be the immediate caprock of the reservoir is about 50-100 m thick, and consist of silty mudstone. The unit above the caprock is coarsening upwards (Chadwick et al., 2004a). When storing in a rock with low permeability the pressure does not have time to stabilize, and this can lead to an overpressure zone close to the injection well (Holloway, 2005).

Trapping mechanisms

Trapping is important to reduce the risk of leakage, and one can have different mechanisms for trapping of CO₂. An effective seal is a required for all different trapping mechanisms. To be an effective seal the rock needs to have low permeability, and the best example is the shale. The most common trapping is the structural and stratigraphic trapping.

The geometry of structural trapping is formed after deposition, and includes structures like anticlines and faults. Stratigraphic trapping geometry is related to the change in lithology, like pinch-out traps and reefs. Residual trapping is another form off trapping, and this phase occurs not long after injection.

The definition of this mechanism is as follows; Small droplets of CO₂ are left behind when the CO₂ migrates inside the reservoir. Over time, the physical and chemical properties of the reservoir play an important part of the storage security (IPCC, 2005). It occurs solubility trapping and mineral trapping.

CO₂ dissolves in water and the water with dissolved CO₂ is denser than the water without CO₂. Due to this, the water with CO₂ sinks down to the bottom of the reservoir, decreasing the possibility of leakage (solubility trapping). After a longer period, the water with dissolved CO₂ will react with minerals in the reservoir rock and create carbonate minerals (mineral trapping). This is the most secure trapping mechanisms to store CO₂, but it takes a very long period of time to reach this. Section from (Halland et al., 2011, Selley, 1998).

Time-lapse seismic monitoring

Monitoring of reservoirs is important to follow the development of fluid migration during production or injection. During production it is beneficial to see where the rest of the hydrocarbons have migrated, to achieve higher recovery numbers.

During injection of CO₂, it is important to see how the plume develops and migrates, to help prevent a possible leakage. It exists several different methods used in time-lapse seismic monitoring, like amplitude changes and AVO/AVA-analysis (Mikkelsen, 2009). I will, as mentioned above, not apply any of these methods, but simply use synthetics and inversion based on the Riccati equation.

During amplitude-based seismic monitoring, is the task to detect differences in seismic anomalies in the new seismic acquisition compared to earlier. This is known as time-lapse seismic and it is the most efficient method in use. Repeated acquisition of seismic data with the same survey parameters is required for this method.

Seismic is based on TWT (two-way-traveltime), and many parameters can influence this time. During production the porosity may change and also the hydrocarbon saturation, and these are parameters affecting the acoustic velocity. During injection of CO₂ the texture of the reservoir may change due to reaction between the CO₂ and surrounding minerals. This will lead to different porosity, and influence the acoustic velocity. The increase of CO₂ saturation will also influence the velocity since the density of CO₂ is lower compared to the surrounding reservoir water. All these things will affect the TWT, and it is not an easy task to exactly determine what is changing the TWT.

Introduction to seismic

I will now introduce seismic that is used to monitor the field. Since CO₂ to tend to migrate upward the subsurface, it is important to watch carefully the behavior of the plume in the study area. I will, as mentioned in the introduction, concentrate on the effect of absorption that is introduced as forward Q-filtering. Seismic inverse Q-filtering (IQF) is one sector of regular inversion technics that employs a wave propagation reversal procedure that compensates for energy absorption and corrects wavelet distortion due to velocity dispersion. When modelling for the inversion we introduce forward Q-filtering (FQF) models, and will give a short description of the background for such models.

Actually, there is a wide range of mathematical definitions of the Q-model presented in the literature, and Wang (2008) summed up about this. A good start is the Kolsky (1953) model that is used extensively in Q-filtering. Wang proposed to modify the Kolsky's basic attenuation-dispersion model. This was primary an attempt to accurately represent the velocity dispersion effect within the seismic frequency band.

Wang writes that if one compares the basic Kolsky model with other different mathematical Q models, one finds that different models were not close to the basic Kolsky model. Wang, by using a modified Kolsky model, was able to derive a set of analytically derived parameters. The primary goal was to make Kolsky's model comparative with a model satisfying a dispersion condition that is necessary to

preserve the causality of a propagating wavelet. Such a dispersion relation is called the Kramers-Krönig dispersion relation. A model of this kind has been discussed by Futterman (1962).

I will use Wang's modification of Kolsky in this article. However, to avoid a rather complicated inverse theory, I will use a least square (LSQ) solution in the Riccati inversion to replace Wang's inverse Q-filtering theory with downward continuation. An attempt with this inversion method without the LSQ-solution was done by Gjevik et al. (1975). In another article Nilsen and Gjevik (1978) presented the theory in a broader way and one absorption model was included. Their theory has been further developed and was presented in two papers on Researchgate. (Sørdsal (2018), Sørdsal (2019)).

Basics of modelling with absorption included

Inverse Q-filtering algorithms are mainly based on forward wave propagation migration type approach. Then the decay of the frequency content due to absorption can be inspected at each time sample. (Wang (2008).) Following Gjevik we can assume monochromatic plane-waves propagating along a vertical axis. Let P define the stress (pressure) and W the displacement. Density is ρ . Newton's second law gives:

$$\frac{dP}{dz} + \rho\omega^2 W = 0 \quad (1)$$

Correspondingly, a stress-strain relationship of the following form is assumed (Hook's law):

$$P = \rho v_r^2 Y \frac{dW}{dz} \quad (2)$$

In Eq.(2) v_r is the reference velocity which could be taken as the group velocity in case of dispersion. The function Y represents depth and frequency-dependent absorption.

In case of no damping, $Y=1$ and Eq.(2) is simply Hookes law.

Combination of Eqs.(1) and (2.b) gives Helmholtz equation (assume constant density)

$$\frac{d^2P}{dz^2} + k^2 P = 0, k = \frac{\omega}{v_r \sqrt{Y}} \quad (3)$$

To achieve a complex damping function we can follow Horton (1959) and introduce the notation

$$Y(\omega, \tau) = A(\omega, \tau) + iB(\omega, \tau) \quad (4)$$

In his paper, Horton gives examples of values of A and B for various absorption models that can be causal or non-causal. Since the wavenumber k is in focus, the following expression is now elaborated on

$$\frac{1}{\sqrt{Y}} = \frac{1}{\sqrt{A+iB}} = \frac{\sqrt{A-iB}}{\sqrt{A^2+B^2}} = \frac{(A^2+B^2)^{1/4} [\cos(u/2) - i \sin(u/2)]}{(A^2+B^2)^{1/2}} = \frac{[\cos(u/2) - i \sin(u/2)]}{(A^2+B^2)^{1/4}}$$

$$\tan(u) = \frac{B}{A} \quad (5)$$

Moreover, the following trigonometric relations are valid

$$\tan(u) = \frac{\sin(u)}{\cos(u)} = \frac{\sin(u)}{\sqrt{1-\sin^2(u)}} = \frac{\sqrt{1-\cos^2(u)}}{\cos(u)} = \frac{B}{A} \Rightarrow \quad (6)$$

$$\cos(u) = \frac{A}{\sqrt{A^2+B^2}}, \quad \sin(u) = \frac{B}{\sqrt{A^2+B^2}}$$

And also these

$$\cos(u/2) = \sqrt{\frac{1+\cos(u)}{2}}, \quad \sin(u/2) = \sqrt{\frac{1-\cos(u)}{2}} \quad (7)$$

Finally, combination of Eqs. (5)-(7) gives the result

$$k = \frac{\omega}{v_r \sqrt{Y}} = \frac{\omega}{v_r \sqrt{A+iB}} = \frac{\omega}{v_r} \left[\frac{1}{\sqrt{A}} - \frac{i}{2} \frac{B}{A\sqrt{A}} \right] \quad (8)$$

Now we will compare the real and imaginary part of k for the Q-models. The real part can be related to the phase velocity and the imaginary part is the attenuation coefficient. Then we have: $k_{real} = \frac{\omega}{v_r} \frac{1}{\sqrt{A}}$

and $k_{imag} = \frac{1}{2} \frac{\omega}{v_r} \frac{B}{A\sqrt{A}}$ (9)

This leads up to different functions A and B that was calculated in Sørdsal (2019) and can be related to Q-models. The outline is also given in appendix 1 and is listed in table 1.

		A	B
1	Kolsky - Wang	$\left[\frac{\omega}{\omega_h} \right]^{2\gamma} \gamma = \frac{1}{\pi Q}$	$\left[\frac{\omega}{\omega_h} \right]^{2\gamma} \frac{1}{Q}$

Table 1. Forward Q-filter

Fig.6. shows \sqrt{A} (which gives us a hint about the dispersion) for Kolsky-Wang. (Multiplying \sqrt{A} with the reference velocity v_r gives us the phase velocity). According to Kolsky, the tuning frequency ω_h should be the smallest frequency in the frequency band and. Wang modified the Kolsky model by choosing the highest frequency in the frequency band. And that will be the Nyquist frequency $2\pi\omega_h = 125$ Hz (blue graph on fig.6.)

For the attenuation coefficient Fig.2. we used $Q=100$ (blue graph) and $Q=50$ (green graph).The attenuation coefficient increase linear with frequency. An important aspect with the Kolsky model is that the attenuation will be strictly linear with frequency over the range of measurement.

From fig.6. we can readily see that more damping (red graph) gives the lower graph. This means that the less damping, the faster will go the reflectors. We will see this when we compute the synthetics.

Attenuation coefficient

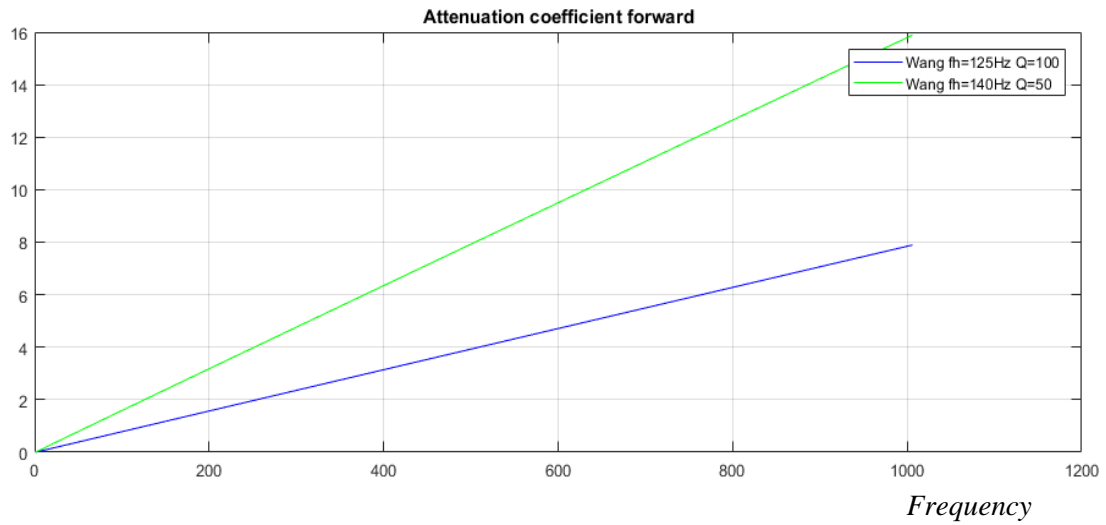


Fig.3. Attenuation coefficient. Attenuation coefficient is dimensioned pr. km or pr.sec.

Phase velocity

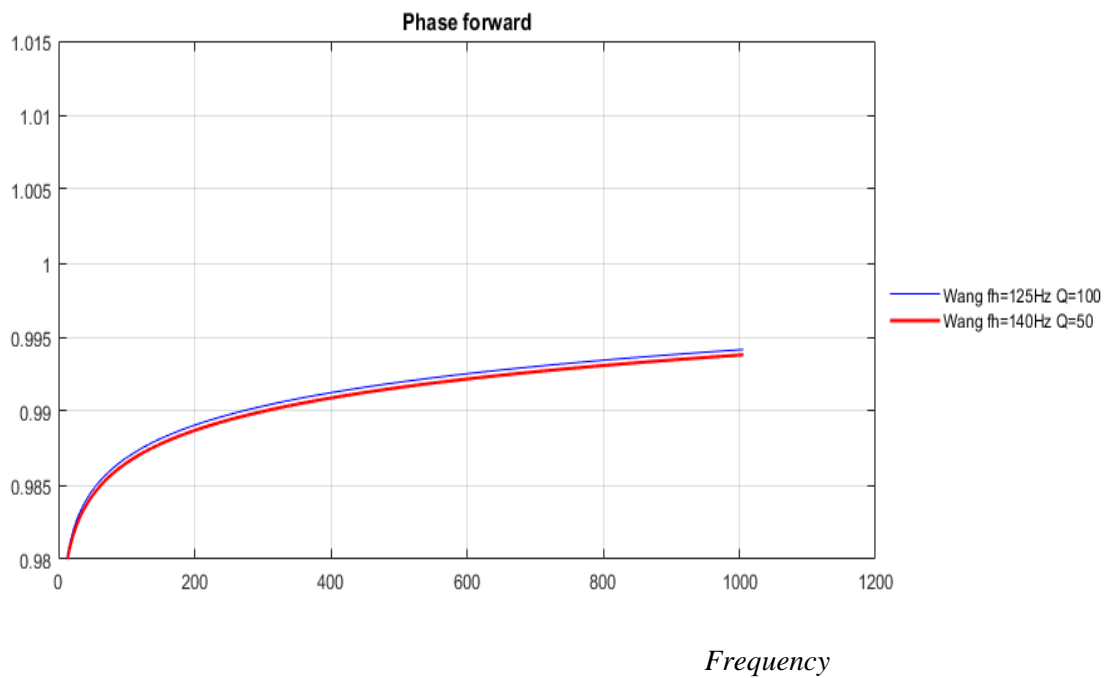


Fig.4. Phase velocity for forward Q -model of table 1. We have used $Q=50$. Wang fh=140Hz (red) Wang fh=125Hz (red) ($w_h=2\pi f_h$), $Q=100$. Phase velocity is dimensionless.

Introducing the Riccati equation with absorption

The basic idea in a downward wave propagation migration approach is that the wavefield at the surface of the seismic earth model is extrapolated down to a depth z . The real part of k in Eq. (9) describes all dispersion effects during wave propagation and the imaginary part describes absorption.

From Nilsen and Gjevik (1978) we have the Riccati equation:

$$\frac{dK}{dz} = \frac{2i\omega}{v_r \sqrt{Y}} K - r(1 - K^2) \quad (10)$$

K is the complex reflection coefficient and r is the depth-dependent 'reflectivity' per depth unity:

$$r(\tau) = \frac{1}{2\rho v_r} \frac{d(\rho v_r)}{d\tau} \quad (11)$$

Since vertically travelling waves are considered, the transformation from depth to two-way traveltime is straightforward

$$\tau = 2 \int_0^z \frac{dz}{v_r}, \Rightarrow d\tau = \frac{2}{v_r} dz \quad (12)$$

Which gives the travel time version of Eq.(10)

$$\frac{dK(\omega, \tau)}{d\tau} = \frac{i\omega}{\sqrt{Y(\omega, \tau)}} K(\omega, \tau) - r(\tau)(1 - K^2), r(\tau) = \frac{1}{2\rho v_r} \frac{d(\rho v_r)}{d\tau} \quad (13)$$

By noticing that

$\exp(-i\omega \int_0^\tau Y(\omega, \tau)^{-1/2} d\tau) \equiv \exp[-\phi(\omega, \tau)]$ is an integrating factor for this Riccati equation, it can

be rewritten on the following form:

$$\frac{d}{d\tau} [K(\omega, \tau) \exp(-\phi(\omega, \tau))] = -r(\tau)(1 - K^2) \exp(-\phi(\omega, \tau)) \quad (14)$$

$$\text{Where } \phi(\omega, \tau) = i\omega \int_0^\tau \frac{d\tau}{\sqrt{Y(\omega, \tau)}} = i\omega \int_0^\tau \left[\frac{1}{\sqrt{A}} - \frac{iB}{2A\sqrt{A}} \right] d\tau = \int_0^\tau \left[\frac{i\omega}{\sqrt{A}} + \frac{\omega B}{2A\sqrt{A}} \right] d\tau \quad (15)$$

Assume now the following boundary condition: $K=0$ when $\tau \geq T$. Integration of Eq. (14) now gives the solution

$$-K(\omega, \tau) \exp(-\phi(\omega, \tau)) = - \int_\tau^T r(\tau') \exp(-\phi(\omega, \tau')) (1 - K^2(\omega, \tau')) d\tau' \quad (16)$$

From Eq.(16) we can, when $K^2 \ll 0$, obtain the non-linear solution

$$K(\omega, \tau) = \exp(\phi(\omega, \tau)) \int_\tau^T r(\tau') \exp(-\phi(\omega, \tau')) (1 - K^2(\omega, \tau')) d\tau' \quad (17)$$

Equation (17) is now the starting point for a non-linear modelling algorithm. Assume a discretization in τ (sample interval $\Delta\tau$ and total of N points), and then start at maximum time $T=(N-1) \Delta\tau$ and then calculate K in upward direction.

We introduce the following notation for convenience

$$\begin{aligned} K_{i,j}^n &= K^n(\omega_i, \tau_j) \quad \tau_j = (j-1)\Delta\tau, \quad j = N-1, N-2, \dots, 1 \\ K_{i,N}^n &= 0 \end{aligned} \quad (18)$$

Where the superscript n implies iteration number.

Next, define (trapezoidal rule applied to integral in Eq.(17)) (assume (n+1) th. iteration)

$$\beta_{i,j} = \frac{\Delta\tau}{2} \left[r_{j+1} X_{i,j+1} \left\{ 1 - (K_{i,j+1}^n)^2 \right\} + r_j X_{i,j} \left\{ 1 - (K_{i,j}^n)^2 \right\} \right], j = N-1, N-2, \dots, 1 \quad (19)$$

$$r_N = 0$$

Which gives the after sought solution

$$K_{i,j}^{n+1} = \beta_{i,j} / X_{i,j}, j = N-1, N-2, \dots, 1 \quad (20)$$

In Eqs.(18 and 19) we have introduced the operator

$$X_{i,j} = \exp \left[-\phi(\omega_i, \tau_j) \right] \tau_j = (j-1)\Delta\tau \quad (21)$$

The seismogram corresponds to the solution $j=1$. The final result in time is obtained after an inverse FFT.

Let the first layer be water, then we need to include the free-surface multiples. Assume that τ_ω represents two-way vertical travel time in the water layer. Total field P_i recorded at the surface (e.g. including multiples) can then be written as (r being the reflection coefficient of the seafloor)

$$P_i = K_{i,j=1} \left[1 - r \exp(-i\omega_i \tau_\omega) + r^2 \exp(-2i\omega_i \tau_\omega) + \dots = \frac{K_{i,j=1}}{1 + r \exp(-i\omega_i \tau_\omega)} \right] \quad (22)$$

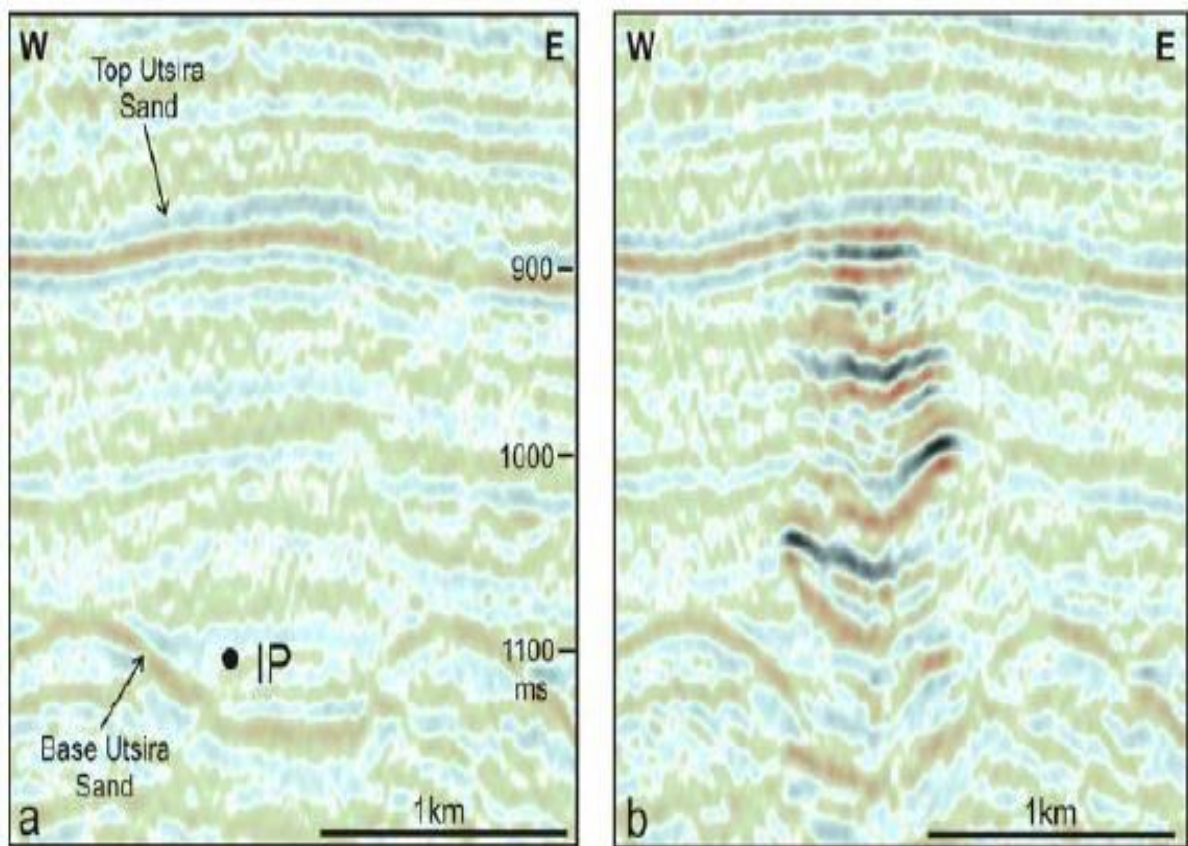


Fig.5. CO2 layers from Utsira sand, Sleipner field

So, both to sum up, and introduce some more details: the Sleipner East field in the North Sea is located 250 km from the coast of Norway (IPCC, 2005). Sleipner East is producing gas/condensate and Sleipner West is producing natural gas, both with Equinor as an operator. The concentrations of CO2 in the natural gas is too high at the Sleipner West field, so they separate the CO2 from the gas before the CO2 is transported by pipeline to the Sleipner East field for injection. Normally they would release the CO2 into the atmosphere, but in 1991 the Norwegian government implemented tax on the CO2 emissions.

Due to this Equinor and the Sleipner partners started injecting CO2 both due to economic and environmental reasons in 1996. The water depth at the injections site is about 80 m (Ghaderi and Landrø, 2009) and the injection point is 1010-1013 m below sea level (Arts et al., 2004a). The injection rate is around 1 million tonnes per year and the goal is to store 20 million tonnes (Chadwick et al., 2004a).

Forward numerical implementation

When we make calculations with the models we need to define $r(\tau)$ from a set of layered model parameters connected to the impedance of a seismic media. We can, of course, get r_j from eq (22) as reflectivity per depth unit (1/s). Invoking Eq.(23) we can calculate two-way traveltimes by converting the layer thickness z into time and using:

$$r(\tau) = \frac{1}{2(\tau_{j+1} - \tau_j)} \left[\frac{\rho_{j+1} V_{j+1}}{\rho_j V_j} - 1 \right] \quad j=1, \dots, NT-1 \quad (23)$$

We can then get R_j (Reflection coefficients) either by setting ρ and v direct into Eq.(24) or setting r from Eq (23) into Eq.(24). Both r and R are similar physical parameters which represents the contrast in acoustic impedance across an interface. To proceed with computations we must discretize every layer in the model with j and move down to the layer $NT-1$. Velocity and density for each layer we find in table 3.

$$R_j = \frac{\rho_{j+1} V_{j+1} - \rho_j V_j}{\rho_{j+1} V_{j+1} + \rho_j V_j} = \frac{\exp[2\Delta\tau r_{j+1}] - 1}{\exp[2\Delta\tau r_{j+1}] + 1} \quad \text{for } j = 0, 1, 2, \dots, NT-1 \quad (24)$$

To set up table 3 for our model parameters we need some data from the Sleipner field for different CO2-saturations. These data we achieved from Nordahl (2015).. The CO2-saturation is important when we study the CO2-plume. Some data are in table 2.a. and studying fig.5, we were able to set up a model roughly with CO2-layers 25 m thick and from fig.7 we could locate maximum saturation and put Q-data into table 3. Figure 7 gave us an idea of absorption as a function of CO2 saturation.

Table.2.a. gives parameters for different CO2-saturations. Fig.6. to the right for the table visualize R for the saturations. Blue color is negative reflector that we can easily calculate from the corresponding values in the table. A lower velocity will give increase in amplitude strength of the reflector. The reason is a decrease in P-velocity denoted v in Eq. (24).

We must understand that the caprock lies above Top Utsira Sand on fig.5. that marks the beginning of the CO2-plume. The interface between the caprock and Top Utsira Sand will be marked with a negative reflector. (blue color). Fig.6. to the left of Table 2.a. shows us the interface for CO2 saturations for 10% to 100%.

The seismic images

CO2-saturation	R (reflection coefficient)	P-velocity (m/s)	Density(kg/m ³)
0 %		2048	2047
10 %	-0,0821	1672	2039
20 %	-0,1175	1568 (1563)	2031
30 %	-0,1363	1511	2022 (2030)
40 %	-0,1476	1482	2014
50 %	-0,1555	1470 (1464)	2006
60 %	-0,1619	1451	1998
70 %	-0,1664	1443	1990
80 %	-0,1705	1437	1982
90 %	-0,1738	1433	1974
100 %	-0,1769	1437	1965 (1966)

Fig.6. To take a closer look at how the seismic amplitude anomalies changes with different CO2 saturation the figure under shows clearly an increase in amplitude strength as the saturation increases. This is expected because of the decrease in acoustic P-velocity from Table 2.a

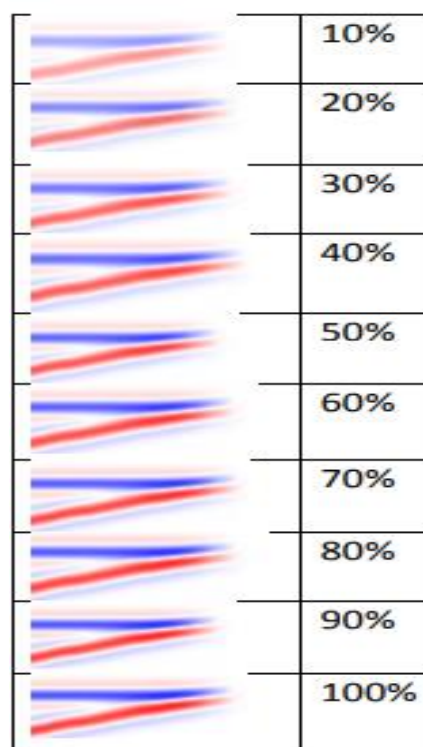


Table 2.a. parameters from Nordahl (2015).

We could also state that the interface between caprock and the plume will be a negative reflection coefficient (blue color) because of transition from a higher impedance to a lower impedance layer. The shale layers inside the reservoir and the plume will be marked with a positive interface (red colors) since we go from a layer with lower impedance to layers with higher impedance. The interface from the thin shale layers back to the plume will then be the opposite, negative reflection coefficient (blue colors). In addition to fig.6 I have illustrated this in table 2.b. with background colors. (Blue color for Utsira sand.)

To sum up: the background model gives us the structure of the sediments without CO2. Different saturations with CO2 will give us different values for velocity and density. This is deviation from the background model. Numbers for the background model can be found in Table 2.b. Also absorption will change for different saturations in table 3. I have given alternative values from background model in yellow color on table 3.

It is important to realize that we consider numbers that are taken from Table 2.a and Table 2.b and roughly estimated from the available numbers. Other numbers will be introduced in other articles in the future. Q-values are estimated from fig.7, but also estimated from values that were usable in the seismic theory.

Layer	P-Velocity (m/s)	Density (kg/m ³)
Water layer (0-80m)	1480	1000
Upper unit (80-720m)	2000-2180	1850-2017
Pliocene Shale (caprock) (720-820)	2180-2360	2017-2183
Utsira sand (820-1030)	1950-2100	1960-2080
Lower unit (1030-2000)	2200-2500	2035-2313

Table 2.b. parameters from Nordahl (2015).

Fig.7 shows us that CO₂-saturation between 5-10% give highest absorption (and lowest Q-values). Therefore we will choose lowest Q-values in most saturated layers (grey colored on Table 3). Fig.7. gives Q about 100 when saturation is near 50 %. However, we will choose less damping to avoid problems with the calculations.

Q	Depth) Layers	Density ρ g/cm ³	Bgr. dens.	Velocity v km/h	Backgr. velocity	Saturation CO ₂	Depth	Layers
Q1=200	80	1.0	1.0	V1=1480	1480	0 %	80	Water layer
Q2=200 100	560	1.5	1.5	V2=1600	1600	45 %	640	Layer 2
Q3=200 100	80	2.0	2.0	V3=2000	2000	45 %	720	Layer 3 Caprock
Q4=200 100	155	2.03	2.0	V4=1800	1800	45 %	875	Layer 4 Caprock
Q5=200 100	25	1.965 2.006	1.966	V5=1437	1470	100%	900	Layer 5
Q6=200 100	25	1.965 2.006	1.5	V6=1437	1500	100%	925	Layer 6
Q7=200	25	2.006 2.03	1.966	V7=1470	1430	50 %	950	Layer 7
Q8=200	25	2.03	1.5	V8=1568	1600	25 %	975	Layer 8
Q9=200	25	1.965	1.966	V9=1430	1430	25 %	1000	Layer 9
Q10=200	25	1.5	1.5	V10=1568	1600	25 %	1025	Layer 10
Q11=200	25	1.96	1.966	V11=2500	2500	25 %	1050	Layer 11

Table 3. Seismic model parameters large model

We choose 2500 m/s for Layer 11, background model that is consistent with Table 2.b. Layer 1 (water layer) is also consistent with Table 2.b. Values for other parameters, however, are chosen in a way that made calculations possible. It will be a challenge for future research to find better agreement between

Table 3 and measurements from Table 2.a. and b. and Q-values from fig. 7. This is the case if layer 3 is the caprock. As mentioned above CO2 in a supercritical phase has the behavior of a gas phase and the volume of a liquid phase. The density of the CO2 will be smaller than the density of the surrounding reservoir water. Due to this the molecules of CO2 will float up in the reservoir (buoyancy effect). Therefore, also the caprock could be saturated with CO2. In table 3 the saturation is estimated to 45 %. We could also regard layer 4 as the caprock with the same CO2-saturation. We could then state that the interface between caprock (layer 4) and the plume (layer 5) will be a negative reflection coefficient (blue color) because of transition from a higher impedance to a lower impedance layer.

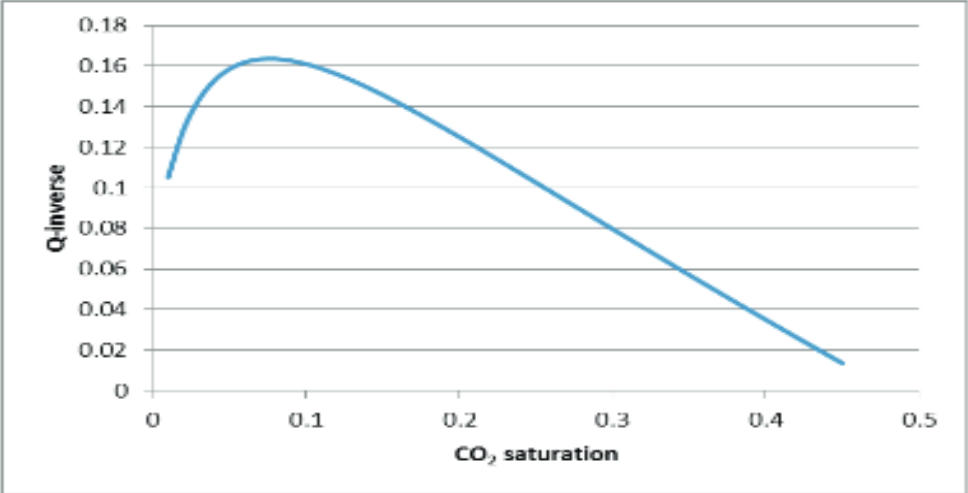


Fig.7 Q-values for CO2 saturation

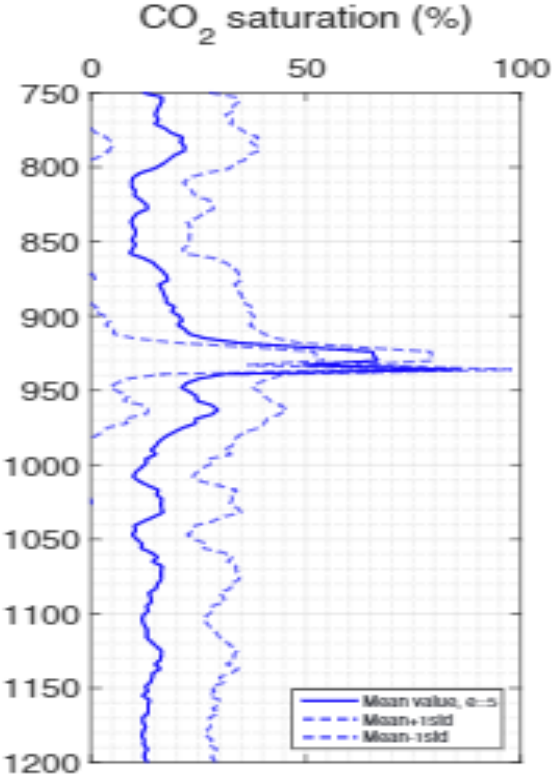


Figure 8. 1D profiles of CO2-saturation estimation taken from Hong Yan (2018). The data is from Utsira sand, Sleipner field. Vertical axes is depth in meters. The CO2-saturation is maximum (estimated 100%) between 900 and 950 meters (marked in table 3).

Values for CO2 in Table 3 are based on roughly estimates from fig.7 and. fig.8. Different saturations with CO2 will give us different parameters for Table 3. Saturation is maximum for depth between 900 and 950 meters and this is marked with grey on Table 3.

Maximum absorption is around 8 % saturation, but table 3 starts with 0% CO2 saturation in the water layer. Fig.7 also shows that CO2-saturation around 45% will give absorption ($1/Q=0,02$). As mentioned above what is important is to find values that were usable in the seismic theory, and we had to try different parameters to get good results, especially for the inversion.

I used some of the data from table 3 for the synthetics Eq.(17). The tables are an attempt to include more accurate data for the section taking also the CO2-saturation into account. The free-surface-multiples were easily introduced and required a water layer (80m depth) above the other layers as introduced in Eq.(22). Density of the water layer is 1 g/cm3 and velocity is 1480 km/h. The synthetics with all multiples are graphs on fig.9.a. from left.

With a background model without attenuation we achieved the synthetics without free-surface-multiples as the black trace on the left fig.9.b. Red graph in same plot is the same synthetics with absorption included. Then we have cplot with both interbed and free-surface multiples. For attenuation we used $Q_1=Q_2=Q_3=200$. We have used the absorption model of Wang with $2\pi\omega_h=140$ Hz. Fig.9.c. looks more closely at the attenuation. We have used lower Q than fig.9.b. However, the seismic model is the same. Left graph with all multiples, right graph without free-surface-multiples. Reflectors are the graph most to the right.

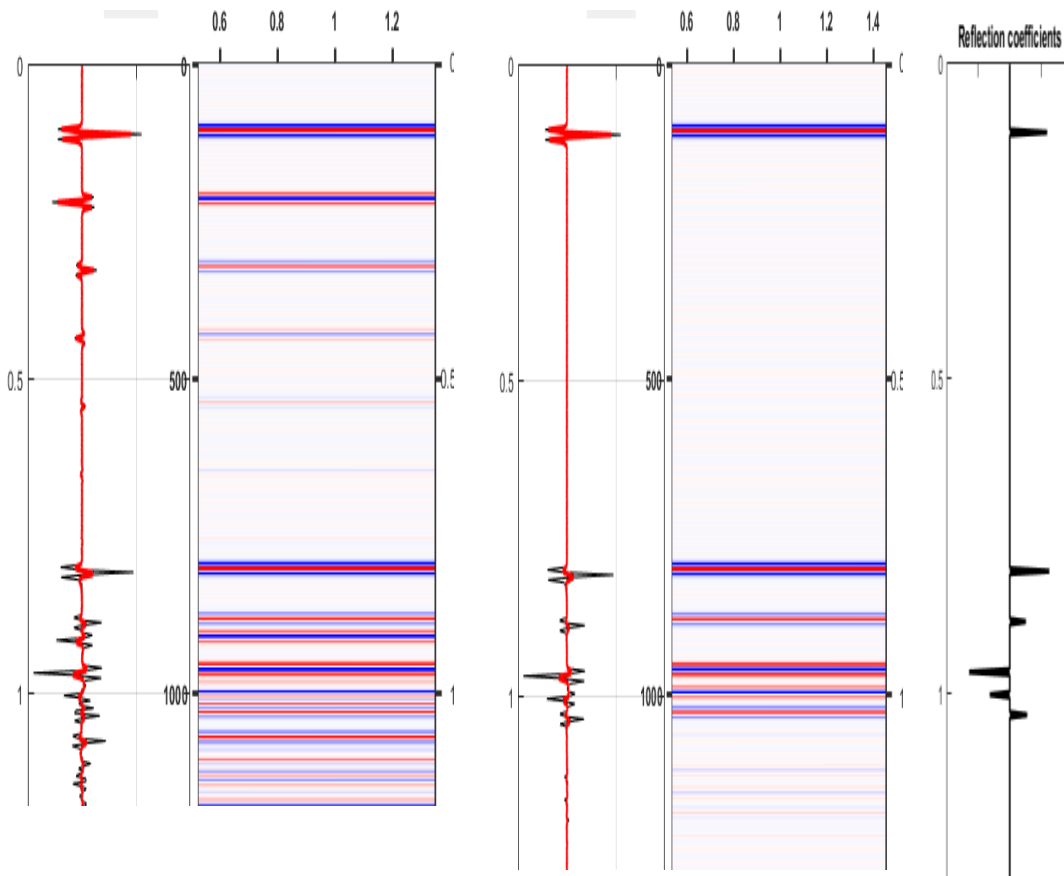


Fig. 9.c. Left graph used $Q_1=Q_2=Q_3=Q_4=Q_5=Q_6=100$. We have used the absorption model of Wang with $\omega_h=2\pi 140$ Hz. All multiples included. The next plot to the right shows synthetics without attenuation (black) and with attenuation (red). $Q_1=100$ $Q_2=70$ $Q_3=70$ $Q_4=Q_5=Q_6=100$ and no multiples. To the right we have reflection coefficients.

First, from left, we have synthetics with all multiples and all Q-values set to 100. Then we have cplot for the background model. Next is synthetics where we have no multiples and more absorption ($Q1=100$ $Q2=70$ $Q3=70$ $Q4=Q5=Q6=100$). An inversion of the synthetics in fig.9a-c should give us the reflection coefficients right.

Before we jump to the inversion, we need to give a remark about the impedance. The relation between r and the impedance makes it possible to compute the impedance for every solution of r . If the acoustic impedance I_0 is known at $z = 0$, (or at any depth), I is also uniquely determined as a function of τ . From Eq. (11) we can deduce:

$$I = I_0 \exp\left(2 \int_0^{\tau} r(\tau) d\tau\right) \quad (25)$$

where $I_0 = \rho_0 v_0$ and I/I_0 will give us a dimensionless relative impedance. We will come back to this in the next section.

Inversion LSQ – inverse numerical implementation

In the following we will implement the layered model parameters (Table 3) that was used to generate the synthetic seismograms in the forward modeling above. The inversion will be done taking the forward modelled synthetic seismograms as input. The procedure will be done with a conventional least square (LSQ) seismic inversion procedure. We will see that an LSQ-inversion is all we need to recover the reflection coefficients from the synthetics .

Consider Eq. (17) in the limit $\tau \rightarrow 0$, which gives the ‘seismogram’

$$K(\omega, 0) = \int_0^T r(\tau') \exp(-\phi(\omega, \tau')) (1 - K^2(\omega, \tau')) d\tau' \quad (26)$$

Introduce ‘reflectivity’ series

$$r(\tau) = \Delta\tau \sum_{i=0}^{NT-1} r_i \delta(\tau - i\Delta\tau), T = NT \cdot \Delta\tau \quad (27)$$

Combination of Eqs. (26) and (27) gives

$$K(\omega, 0) = \sum_{i=0}^{NT-1} r_i \exp(-\phi(\omega, i\Delta\tau)) (1 - K^2(\omega, i\Delta\tau)) \Delta\tau \quad (28)$$

Originally, seismogram recorded in timedomain, i.e. $k(t, 0)$, and assume sampled with a total of NT -samples. Fourier transform of the data will give the same number of monochromatic seismograms.

Nilsen and Gjevik introduced an iterative inversion procedure to solve for r in eq.(26) when the reflection response of the reflecting layer is known. When absorption was included that could be a complicated process and as far as we know no calculations were done with absorption by them.

Leiv Gelius, in an unpublished note, suggested a more elegant solution of the equation with the matrix system:

$$\begin{bmatrix} K_{n+1}(\omega_0, 0) \\ K_{n+1}(\omega_1, 0) \\ \vdots \\ K_{n+1}(\omega_{NT-1}, 0) \end{bmatrix} = \quad (29)$$

$$\begin{pmatrix} \exp(-\varphi(\omega_0, 0)(1 - K_{0,n}^2) & \exp(-\varphi(\omega_0, \Delta\tau)(1 - K_{1,n}^2) & \dots & \exp(-\varphi(\omega_0, (NT-1)\Delta\tau)(1 - K_{n,n}^2) & r_{n,0} \\ \exp(-\varphi(\omega_1, 0)(1 - K_{0,n}^2) & \exp(-\varphi(\omega_1, \Delta\tau)(1 - K_{1,n}^2) & \dots & \exp(-\varphi(\omega_1, (NT-1)\Delta\tau)(1 - K_{n,n}^2) & r_{n,1} \\ \vdots & \vdots & \dots & \vdots & \vdots \\ \vdots & \vdots & \dots & \vdots & \vdots \\ \exp(-\varphi(\omega_{NT-1}, 0)(1 - K_{0,n}^2) & \exp(-\varphi(\omega_{NT-1}, \Delta\tau)(1 - K_{1,n}^2) & \dots & \exp(-\varphi(\omega_{NT-1}, (NT-1)\Delta\tau)(1 - K_{n,n}^2) & r_{n,NT-1} \end{pmatrix}$$

Hagos (2016) made some computations for Eq.(29) in his thesis. A more detailed study of the solution is in appendix 2. The mathematics for how to do least square inversion is also outlined in Sørdsal (2018).

Note that $K_0^2=0$ in the first iteration. After a new estimate of the reflectivity series has been obtained, an update of $K_{i,n}^2$ can be obtained by solving the forward problem. Iterations are carried out until the relative change in reflectivity is below a certain user threshold. The effect of the inversion when $K^2 = 0$ is simply to compensate for the damping of the amplitude caused by attenuation and correct the phase term caused by dispersion. When $K^2 < 0$ we also remove multiples and compensate transmission loss. Surface multiples can also be removed simply by multiplying K with the inverse of RHS of Eq (22). First we remove surface multiples before we solve Eq.(29). This can simply be done multiplying r with the inverse of Eq. (22). Fig.10 shows both the synthetics (Eq.17) and the inversion Eq.(29) with the synthetics r as input. I took the first plot (red) from left on fig.9 as input. The inversion (middle plot) gives us a sharp layer (blue). Right plot from middle plot shows the impedance and then the reflector model. When we change velocity V_4 from 2400 till 2000, we achieve the change that can be seen on the impedance. The inversion will not correct change due to change in velocity.

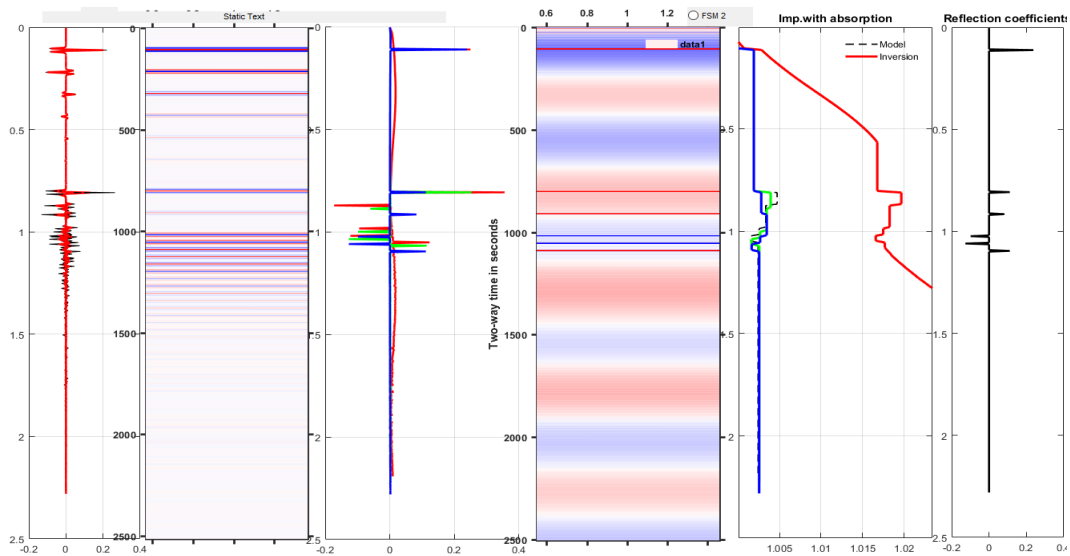


Fig.10.v3:1480,1600,X,1800,1430,1500,1430,1500 red:X=2500, green:X=2000 blue:X=1500

$Q_2=200$ for all layers

To go back to fig.9.b . where we could easily see the fourth reflector differs in colors (left (negative red)) right (positive blue) due to the change from 2500 to 1800 for V4. The inversion had some problems with the red graph giving V4=2500. Changing from 2500 to 1800, the inversion is much better. This can be seen on fig.11. Gjevik (1976) mentioned about this. High contrast in impedance could give problems to the inversion. Fig.11. gives a smooth transition from a lower velocity than in fig.10. And the inversion converges. We got an inversion more similar to the synthetics on fig.9.b. The most simple way to see this is to compare the dotted line in the impedance inversion on graph five with fig.11 with the red graph in the same plot. They are indistinguishable from each other.

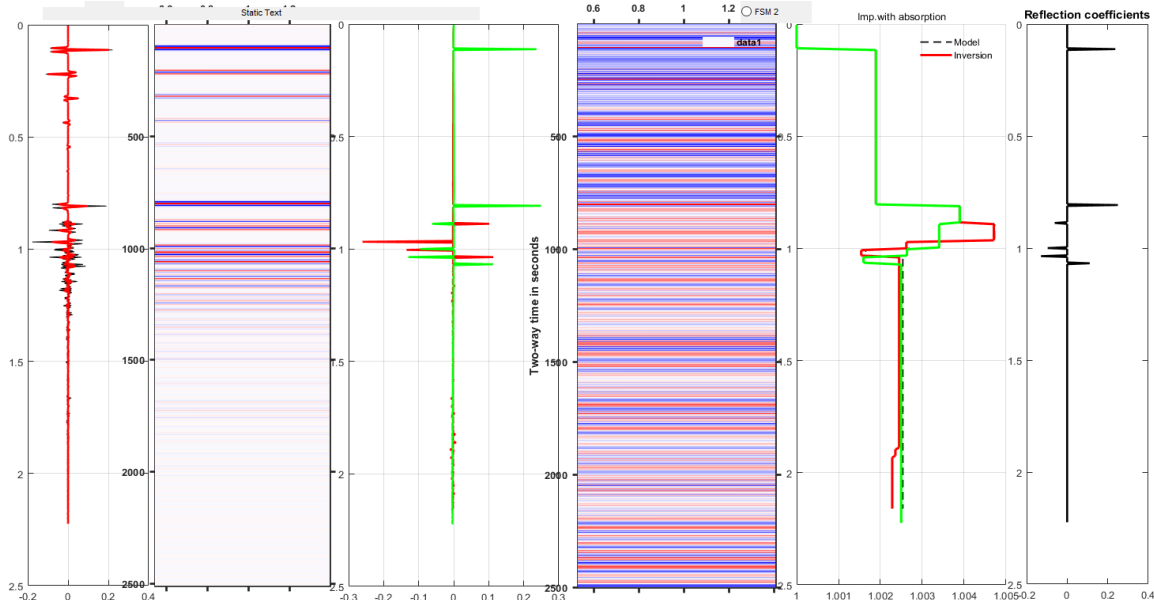


Fig.10 From left: synthetics, Third graph from left: Inversion and cplot of inversion, and then impedance inversion, red graph: V4=2500, green graph: V4=1800, Q=200 for all layers. Right graph is reflectors.

Fig.9-10 shows calculations with data from the first 6 reflectors. Will we get more problems using more reflectors?

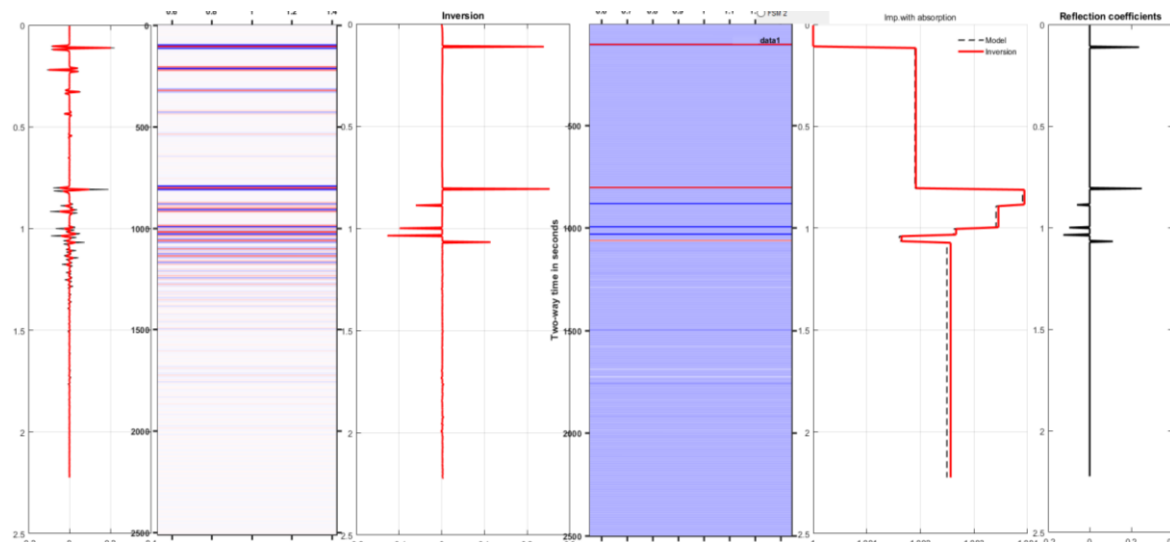


Fig.11. V=1480,1600,2000,1800,1437,1500,1430. Red and black dotted graph in impedance inversion is indistinguishable from each other.

On fig.11. we have more reflectors in the model that was introduced on fig.10. Left is synthetics where red graph is with attenuation and black is without. Then we have cplot synthetics. So we have inversion, red is high impedance ($V_4=2500$) and green is low impedance ($V_4=1800$). We can see a change in the inversion due to change in impedance and this is shown as a delay in the arrivals. This change is introduced in the synthetics and is not corrected for in the inversion. Our theory will not correct delays due to impedance change. However, it will correct delays caused by dispersion from absorption. This important aspect of the theory will be discussed in my next article.

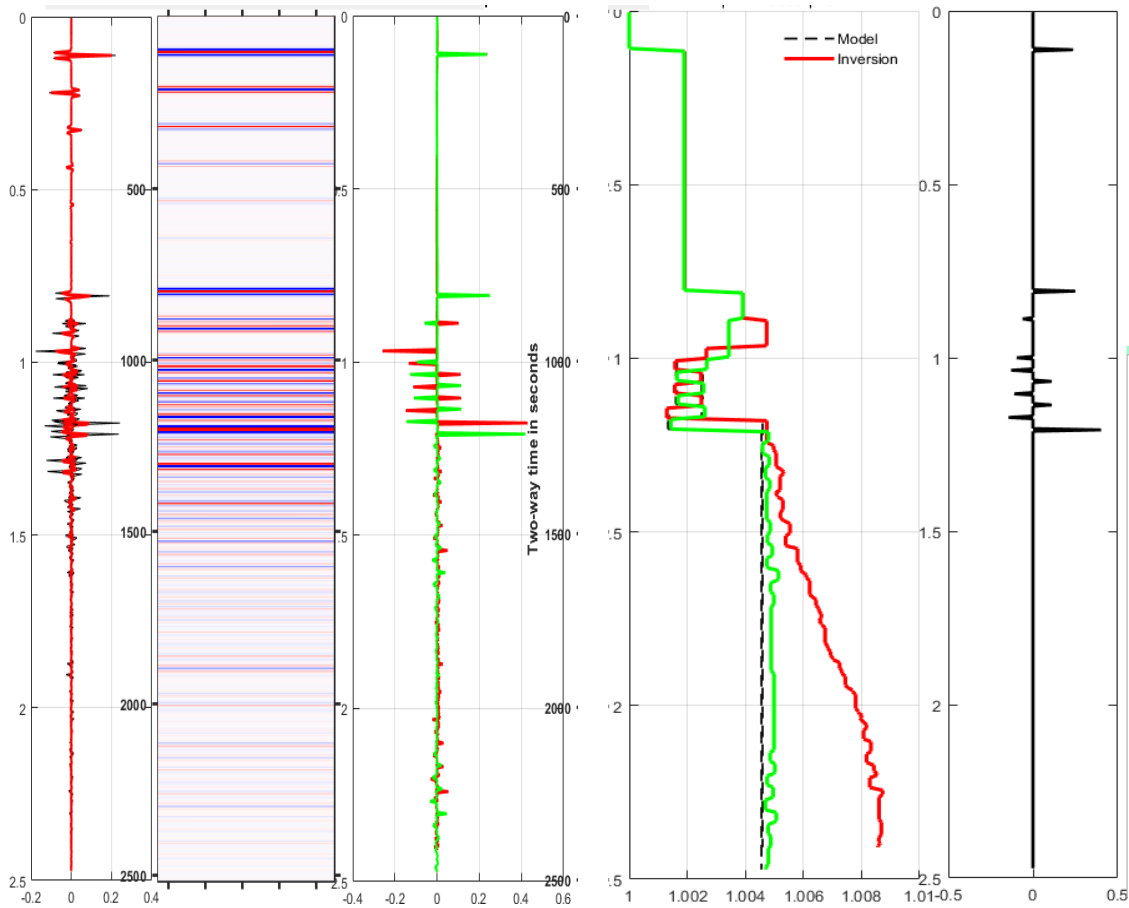


Fig.12. From left: synthetics, Third graph from left: Inversion, and then impedance inversion, red graph: $V_4=2500$, green graph: $V_4=1800$, $Q=200$ for all layers. Right graph is reflectors.

A closer look at the inversion

Ultimately, after the development of the previous theory we have been able to combine a forward solution of Kolsky-Wang Q-filter with a LSQ-solution for inversion. So we have fulfilled the purpose of this article. However, a broader view of the subject could be interesting in the future and a further study of Q-filtering is necessary as well as more studies of velocity change.

So, to even further sum up: setting $K^2=0$ in eq (29) we achieved the linear solution on matrix form and solved this for r as a time-domain vector that represents the filter. The inverse Q-filtering procedure was performed successively to each time sample to get the time-dominant output vector. We then used the output r as input getting the inverted solution for a new inverted r .

When we do this we can, of course, replace the Q-filters with the inverse Q-filters as Wang did, and this could be a further study. Then we also will need to study the stabilization of the inverse filter, gain limitation and so on. However, the LSQ-solution in this paper simplified the study. A more complicated theory for the LSQ-solution are introduced in appendix 2. It is called the regularization of the LSQ-solution. It was not necessary to introduce regularization in this study, to achieve the goal of the paper, but could be a subject for further study.

Further iterations in the Riccati-solution introduced non-linearity on the way to a seismic theory that can be used on real data and will be, as far as I can see, a broader and better theory than the theory of Wang that was strictly linear. And, of course, the application of the theory applied on CO₂-monitoring is more relevant in today's world than traditional seismic for oil prospecting. I have also shown that CO₂ in the seismic structure will introduce some problems that will be complicated to solve. Velocity changes in the CO₂-saturated structure compared to the background model will introduce problems in addition to problems caused by absorption.

Conclusion

The results of the preceding sections show that the Riccati equation with Q-filtering provides a method for the construction of synthetic reflection seismograms that is a continuation of the method introduced by Nilsen and Gjevik. Moreover does this theory describe a method for inverting reflection data, i.e. computing the variations in the acoustic impedance within a reflecting layer that can be used in real prospecting. This I have briefly suggested by introducing a water layer over a more complicated seismic model from the Sleipner field. And the Riccati inversion corrects phase, compensates frequency loss, removes multiples and compensates transmission loss in one single process. However it does not correct for phase change due to CO₂.

In my previous articles I tested the abilities of the inversion method by inverting a synthetic reflection seismograms computed from a simple impedance model with a water layer. And this article introduce so much more that concerns real seismic prospecting. We have seen the application of the theory on a more complex structure. Some new problems that has never been discussed before has arrived and must be discussed in the future.

References

Gjevik et al. (1976) *An attempt at the inversion of reflection data. Geophysical prospecting* 24,492-505

Nilsen and Gjevik (1978): *Inversion of reflection data. Geophysical prospecting* 26, 421-432

Yanghua Wang (2008) *Blackwell Publishing. Seismic inverse Q filtering*

Knut Sørdsal (1981) *Viskoelastiske dempningsmodeller i Riccatiligningen anvendt i marin seismikk. University of Oslo*

Knut Sørdsal (2019) *Seismic Q-filter models applied to the Riccati equation*
https://www.researchgate.net/publication/337682839_Seismic_Q-filter_models_applied_to_the_Riccati_equation

Knut Sørdsal (2018) *1-D non-linear inversion of data with absorption - revisited.*
https://www.researchgate.net/publication/331257025_1-D_non-linear_inversion_of_data_with_absorption_-_revisited

Bland(1960) *The theory of linear viscoelasticity. Pergamon Press*

Horton (1959) *A loss mechanism for the Pierre Shale. Geophysics vol.24, no 4*

- Aki and Richards (2002) Quantitative Seismology W.H. Freeman and Co. San Fransisco*
- Kolsky, 1956 The propagation of stress pulses in viscoelastic solids. Philosophical Magazine 1, 693-710*
- Kjartansson E. 1979 Constant Q wave propagation and attenuation. Journal of Geophysical Research 84 4737-48.*
- Futterman W.I 1962 Dispersive body waves. Journal of Geophysical Research 67 , 5279-91*
- Trorey A.W, 1962 Theoretical seismograms with frequency and depth dependent absorption. Geophysics 27, 766-85*
- Claerbout J.F.1976 Fundamentals of Geophysical Data Processing. McGraw-Hill Book Co. New York*
- Hagos Geberehiwet Gebregergs (2016): Compensation of Absorption Effects in Seismic Data. University of Oslo*
- Hong Yan, Bastien Dupuy, Anouar Romdhane and Børge Arntsen Geophysical Prospecting, 2019, 67, 1055–1071 CO₂ saturation estimates at Sleipner (North Sea) from seismic tomography and rock physics inversion*
- Janita Louise Nordahl : (2015) Modeling of seismic amplitude anomalies associated with CO₂ underground storage — EOM-3901 Master's Thesis in Energy, Climate and Environment*
- KARSTENS, J. & BERNDT, C. 2015. Seismic chimneys in the Southern Viking Graben – Implications for palaeo fluid migration and overpressure evolution. Earth and Planetary Science Letters, 412, 88-100.*
- HALLAND, E. K., JOHANSEN, W. T. & RIIS, F. 2011. CO₂ Storage Atlas Norwegian North Sea, Norwegian Petroleum Directorate.*
- ARTS, R., EIKEN, O., CHADWICK, A., ZWEIGEL, P., VAN DER MEER, B. & KIRBY, G. 2004a. Seismic monitoring at the Sleipner underground CO₂ storage site (North Sea). Geological Society, London, Special Publications, 233, 181-191.*
- ARTS, R., EIKEN, O., CHADWICK, A., ZWEIGEL, P., VAN DER MEER, L. & ZINSZNER, B. 2004b. Monitoring of CO₂ injected at Sleipner using time-lapse seismic data. Energy, 29, 1383-1392.*
- Hiroyuki Azuma (2014) Utilization of seismic attenuation in the monitoring of CO₂ geological storage project. Science Direct.*
- HALLAND, E. K., JOHANSEN, W. T. & RIIS, F. 2011. CO₂ Storage Atlas Norwegian North Sea, Norwegian Petroleum Directorate.*
- BRUANT, R. G., GUSWA, A. J., CELIA, M. A. & PETERS, C. A. 2002. Safe storage of CO₂ in deep saline aquifers. Environmental Science & Technology, 36, 240A-245A*
- PRUESS, K. 2008. On CO₂ fluid flow and heat transfer behavior in the subsurface, following leakage from a geologic storage reservoir. Environmental Geology, 54, 1677-1686.*
- BÜNZ, S., FAVEROLA, A. & PANIERI, G. 2014. Lecture notes in GEO-3151 Seminar in Energy and Environment.*
- BENTHAM, M. & KIRBY, M. 2005. Stockage du CO₂ dans les aquifères salins. Oil & Gas Science and Technology - Rev. IFP, 60, 559-567.*

CHADWICK, A., ARTS, R., BERNSTONE, C., MAY, F., THIBEAU, S. & ZWEIGEL, P. 2008. *Best practice for the storage of CO2 in saline aquifers - observations and guidelines from the SACS and CO2STORE projects.*, Nottingham, UK. (British Geological Survey Occasional Publications, 14).

CHADWICK, A. & WILLIAMS, G. 2010. *Quantitative analysis of time-lapse seismic monitoring data at the Sleipner CO2 storage operation.* *The Leading Edge*, 29, 170-177.

CHADWICK, R. A., ARTS, R., EIKEN, O., KIRBY, G. A., LINDEBERG, E. & ZWEIGEL, P. 2004a. *4D Seismic Imaging of an Injected CO2 Plume at the Sleipner Field, Central North Sea.* *Geological Society, London, Memoirs*, 29, 311-320.

CHADWICK, R. A., ZWEIGEL, P., GREGERSEN, U., KIRBY, G. A., HOLLOWAY, S. & JOHANNESSEN, P. N. 2004b. *Geological reservoir characterization of a CO2 storage site: The Utsira Sand, Sleipner, northern North Sea.* *Energy*, 29, 1371-1381.

SELLEY, R. C. 1998. *Elements of Petroleum Geology*

Appendix 1

In the literature the wavenumber k is often written on the following form in case of absorption (constant-Q model)

$$k = \frac{\omega}{v(\omega)} \left[1 - \frac{i}{2Q} \right] = \frac{\omega}{v_r} + \left[\frac{\omega}{v(\omega)} - \frac{\omega}{v_r} \right] - i\alpha(\omega) = \frac{\omega}{v_r} + \varphi(\omega) - i\alpha(\omega). \quad \alpha = \frac{\omega}{2Qv(\omega)} \quad (\text{A.1})$$

Where α is the absorption coefficient and φ is the phase of the ‘absorption filter’. In order to ensure causality, the filter should be minimum phase. For such a filter this relationship holds.

$$\varphi(\omega) = H[\alpha(\omega)]$$

With H denoting the Hilbert Transform. In case of no dispersion ($\varphi=0$), the filter will be noncausal. Then we have

$$k = \frac{\omega}{v_r \sqrt{Y}} = \frac{\omega}{v_r \sqrt{A + iB}} = \frac{\omega}{v_r} \left[\frac{1}{\sqrt{A}} - \frac{i}{2} \frac{B}{A\sqrt{A}} \right] \quad (\text{A.2})$$

Equating Eqs. (A.1) and (A.2) gives the relationships

$$A = \left[\frac{v(\omega)}{v_r} \right]^2 \quad B = \left[\frac{v(\omega)}{v_r} \right]^2 \frac{1}{Q}, \quad (\text{A.3})$$

Aki and Richards (2002) show that the following relation should be held to honor causality

$$\frac{\omega}{v(\omega)} - \frac{\omega}{v_\infty} = H \left[\frac{\omega}{2Qv_\infty} \right] \quad (\text{A.4})$$

Where v_∞ is the limit of the velocity function when ω tends to infinity. Equation (12) can be further approximated as

$$\frac{\omega}{v(\omega)} - \frac{\omega}{v_h} \cong H \left[\frac{\omega}{2Qv_\infty} \right] \quad (\text{A.5})$$

Where v_h is the velocity related to the highest possible (tuning) frequency of the seismic band. The wavenumber is accordingly adjusted as (compare with Eq.(A.1)).

$$k = \frac{\omega}{v_h} + \left[\frac{\omega}{v(\omega)} - \frac{\omega}{v_h} \right] - i \frac{\omega}{2Qv(\omega)} = \frac{\omega}{v_h} \left\{ 1 + \left[\frac{v_h}{v(\omega)} - 1 \right] - i \frac{v_h}{2Qv(\omega)} \right\} \quad (\text{A.6})$$

And combined with a Kolsky type of phase-velocity model (Kolsky, 1956)

$$v(\omega) = v_h \left(\frac{\omega}{\omega_h} \right)^\gamma, \quad \gamma = (\pi Q)^{-1} \quad (\text{A.7})$$

Gives the wavenumber model

$$k = \frac{\omega}{v_h} \left[1 + \left[\left(\frac{\omega}{\omega_h} \right)^{-\gamma} - 1 \right] - \frac{i}{2Q} \left(\frac{\omega}{\omega_h} \right)^{-\gamma} \right] \quad (\text{A.8})$$

Which has been employed by Wang. From Eqs. (A.1) and (A.2) it also follows that ($v_r=v_h$)

$$A_{Wang} = \left[\frac{\omega}{\omega_h} \right]^{2\gamma} B_{Wang} = \left[\frac{\omega}{\omega_h} \right]^{2\gamma} \frac{1}{Q} \quad (\text{A.9})$$

From Eq.(A.9) it follows that $0 < A_{Wang} < 1$, and the same for B_{Wang} but with $B_{Wang} \ll A_{Wang}$.

Based on Eq. (A.3), Kjartansson (1979) proposed an alternative wavenumber model

$$k = \frac{\omega}{v_\infty} + \left[\frac{\omega}{v(\omega)} - \frac{\omega}{v_\infty} \right] - i \frac{\omega}{2Qv_\infty} = \frac{\omega}{v_\infty} + H \left[\frac{\omega}{2Qv_\infty} \right] - i \frac{\omega}{2Qv_\infty} \quad (\text{A10})$$

From Eqs.(11) and (A.10) it follows that ($v_r=v_\infty$)

$$A_{Futt} = \left[1 + \frac{1}{\omega} H \left(\frac{\omega}{2Q} \right) \right]^{-2} B_{Futt} = (A_{Futt})^{3/2} \frac{1}{Q} \quad (\text{A.11})$$

For completeness, we also have the dispersion-free and non-causal absorption model of Futterman (1962), which corresponds to

$$A_{Futt} = 1 \quad B_{Futt} = \frac{1}{Q} \quad (\text{A.12})$$

Ricker wavelet in the synthetics

In order to get the synthetic seismogram in time domain by inverse Fourier transform of the complex reflection coefficient K, each component of K (Eq.(26) is multiplied by a sampled Ricker wavelet in frequency domain:

$$Sr_w = (2/(\text{sqrt}(\pi))) \frac{f^2}{f_c^3} \exp\left(-\frac{f}{f_c}\right)^2 \quad (\text{A.13})$$

This Ricker wavelet is a zero-phase wavelet and is non-causal. The frequency f_c is called the center frequency and will vary.

Appendix 2

To apply least-square inversion, Eq. (29) can be written in vector and matrix notation in short as

$$\vec{K} = M \vec{r} \quad (\text{A14})$$

where

$$\vec{K} = \begin{bmatrix} K_{n+1}(\omega_0, 0) \\ K_{n+1}(\omega_1, 0) \\ \vdots \\ K_{n+1}(\omega_{NT-1}, 0) \end{bmatrix} \quad \vec{r} = \begin{bmatrix} r_{n,0} \\ r_{n,1} \\ \vdots \\ r_{n,NT-1} \end{bmatrix}$$

$$M = \Delta\tau \begin{pmatrix} \exp(-\varphi(\omega_0, 0)(1-K_{0,n}^2)) & \exp(-\varphi(\omega_0, \Delta\tau)(1-K_{1,n}^2)) & \dots & \exp(-\varphi(\omega_0, (NT-1)\Delta\tau)(1-K_{n,n}^2)) \\ \exp(-\varphi(\omega_1, 0)(1-K_{0,n}^2)) & \exp(-\varphi(\omega_1, \Delta\tau)(1-K_{1,n}^2)) & \dots & \exp(-\varphi(\omega_1, (NT-1)\Delta\tau)(1-K_{n,n}^2)) \\ \vdots & \vdots & \dots & \vdots \\ \vdots & \vdots & \dots & \vdots \\ \exp(-\varphi(\omega_{NT-1}, 0)(1-K_{0,n}^2)) & \exp(-\varphi(\omega_{NT-1}, \Delta\tau)(1-K_{1,n}^2)) & \dots & \exp(-\varphi(\omega_{NT-1}, (NT-1)\Delta\tau)(1-K_{n,n}^2)) \end{pmatrix} \quad (\text{A15})$$

\vec{K} is a (Nx1) vector, M is a (NxN) matrix and \vec{r} is a (Nx1) vector. Let \vec{K} be the desired seismic output data while the actual output from Eq. (A14) is $\vec{S} = M \vec{r}$. We want to compute a reflectivity per depth unit series \vec{r} such that the difference $\vec{\Sigma}$ between the actual output \vec{S} and the predicted seismic output data \vec{K} is minimum in the least square sense. Therefore, the error $\vec{\Sigma}$ with respect to parameter vector \vec{r} is $\vec{\Sigma} = \vec{K} - \vec{S} = \vec{K} - M\vec{r}$. And the cumulative squared error:

$$\begin{aligned} \vec{\Sigma}^T \vec{\Sigma} &= (\vec{K} - M\vec{r})^T * (\vec{K} - M\vec{r}) = \\ &(\vec{K}^T * \vec{K} - \vec{K}^T M\vec{r}) - \vec{r}^T M^T K^T + (\vec{r}^T M^T * M\vec{r}) \end{aligned} \quad (\text{A16})$$

Where T denotes matrix transpose and * denotes complex conjugate.

We want to estimate a reflectivity per depth unit series \vec{r} such that the quantity $\vec{\Sigma}^T \vec{\Sigma}$ is minimum. This condition leads to setting the derivative of $\vec{\Sigma}^T \vec{\Sigma}$ with respect to \vec{r} to zero. Differentiate both sides of eq. (A16) with respect to \vec{r} and observe the requirement for least square procedure minimization that

$$\frac{\delta \vec{\Sigma}^T \vec{\Sigma}}{\partial \vec{r}} = -\vec{K}^T * M + \vec{r}^T * M^T * M = 0 \quad (\text{A17})$$

Because \vec{r}^{T*} is complex valued, $\frac{\delta \vec{r}^{T*}}{\delta \vec{r}} = 0$. Thus applying matrix transpose and rearranging the terms of eq. (A17)

$$\begin{aligned} (M^T * M)^T * \vec{r} &= M^T \vec{K} \Rightarrow (M^T M) \vec{r} = M^T * \vec{K} \\ \Rightarrow \vec{r} &= (M^T * M)^{-1} M^T \vec{K} \end{aligned} \tag{A18}$$

Eq (A18) will give us the reflectivity per depth unit and from this we can calculate the impedance.

Damping constant when calculating reflectivity

To further understand the inversion we need to discuss how reflectivity per depth unit is computed and the introduction of the matrix M defined in Eq.(A14). However an important aspect must be discussed first. The singularity of the matrix $M^T * M$ makes it necessary to introduce a damping constant λ when calculating r. This λ is chosen out from the ‘singular value decomposition’ (svd) of the matrix $M^T * M$. Now we get an invertible new matrix:

$$L = \text{svd}(M^T * M) \text{ giving } M^T * M + \lambda I$$

I is a unitary matrix of the same order as the matrix $M^T * M$

$$\begin{aligned} (M^T * M)^T * \vec{r} &= M^T \vec{K} \Rightarrow (M^T M) \vec{r} = M^T * \vec{K} \\ \Rightarrow \vec{r} &= (M^T * M)^{-1} M^T \vec{K} \end{aligned} \tag{A.19}$$

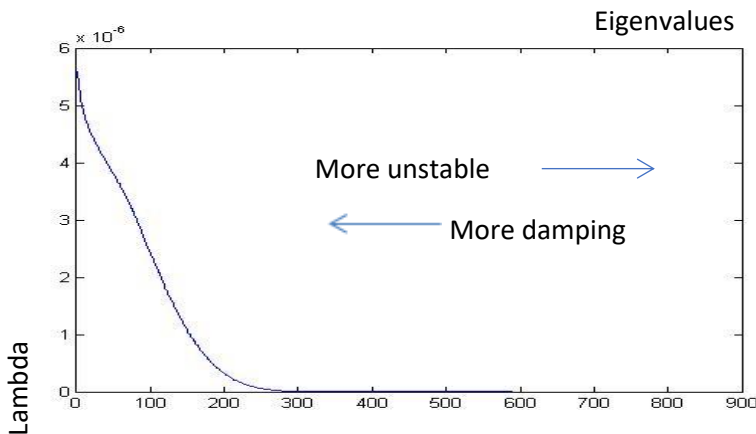


Fig.A.1 .Damping constant lambda as a function of the eigenvalues of $M^T * M$

We will choose lambda around (NT/2) eigenvalue of the matrix $M^T * M$ to be able to use it in the inversion. The output reflectivity (r) will then depend on the value of lambda and introduce damping.

Fig.A.1 shows that when we choose smaller eigenvalues lambda will increase and r is more damped. When lambda increase we found that the effect of the inversion was less and over a threshold value no effect at all. When we increase eigenvalues, lambda decrease. Then we get less damping but r is also more unstable, and can introduce noise. For all calculations in our article we choose lambda=4.8.

It should be taken care to choose the right damping constant (λ) in order to perform the inversion. The choice must be related to noise level, choice of Butterworth filtering and scaling until one gets a satisfying result. We have not discussed this here, but plan to do it in future research.